Boolean Lithography for Volumetric Additive Manufacturing

Authors: Chaofan He[1,2,†], Qilin Wu[1,2,†], Qixiang Yang[1,2,†], Yan Gao[3,†], Xue Zhang[4], Guofeng Liu[1,2] Tianhong Qiao[1,2], Yuan Sun[1], Jianhua Zhang[1], Huayonog Yang[1,*], Yong He[1,2,5,*]

Affiliations:

[1]State Key Laboratory of Fluid Power and Mechatronic Systems & Liangzhu Laboratory, School of Mechanical Engineering, Zhejiang University, Hangzhou 310027, China
[2]Zhejiang Key Laboratory of Additive Manufacturing Technology and Equipment, College of Mechanical Engineering, Zhejiang University, Hangzhou 310027, China
[3]Liangzhu Laboratory, Zhejiang University, Hangzhou, 311121, China
[4]College of Medical Imaging, Qilu Medical University, Zibo, Shandong, 255300, China
[5]The Second Affiliated Hospital of Zhejiang University, Zhejiang University, Hangzhou 310027, China
†These authors contributed equally to this work.
*Corresponding author. Email: yhy@zju.edu.cn (H. Y.), yongqin@zju.edu.cn (Y.H.).

Abstract: Volumetric additive manufacturing (VAM) offers unprecedented production speeds; however, its need for deep optical penetration entails severe background exposure and light scattering, limiting its achievable resolution. Here, we present Boolean Lithography (BL), enabling *in situ* synchronous "additive-subtractive" manufacturing via an "AND-NOT" logic synergy between initiation and inhibition light fields. Specifically, custom positive-negative projections govern the "AND" logic, while a newly identified electrostatic-enhanced single-electron transfer (EE-SET) mechanism mediates the "NOT" logic. By mitigating parasitic exposure, BL broadens the printable window by 201%, achieving optical-resolution-level printing precision, 3×3×3 spatial arrays, and printability in high-scattering inks (180 NTU). Applicable across aqueous and oleaginous systems, BL provides a scalable strategy for high-precision microfabrication and resolution enhancement in other light-scattering-limited optical processing technologies.

Main Text:

Light, owing to its ultrafast response, medium-free propagation, and facile spatial manipulability, has consistently served as a core modality in precision manufacturing. Photopolymerization-based additive manufacturing technologies, such as stereolithography (SLA)(*1*), digital light processing (DLP)(*2*), and two-photon polymerization (TPP)(*3*), have also been widely adopted across fields including biomedicine(*4*), micro/nano-fabrication(*5*), and industrial manufacturing(*6*). However, constrained by the layer-by-layer deposition principle, their efficiency remains insufficient for mass production. Volumetric additive manufacturing (VAM) techniques such as computed axial lithography (CAL)(*6*) synthesize 3D light fields via multi-angle projections to fabricate entire objects simultaneously(*7*), compressing printing times to tens of seconds(*8*).

However, present VAM methods still face an intrinsic physical bottleneck rooted in the spatiotemporal accumulation of light dose. As the light field penetrates the entire printing vat to construct 3D structures, the unavoidable accumulation of background dose triggers unintended photopolymerization in non-target regions(*9*) (fig. S1). More severely, in traditional layer-by-layer methods, the thin curing slices (50-100 μm) permit the addition of photoabsorbers to suppress light scattering(*10-12*). By contrast, VAM requires deep optical penetration across centimetre-scale volumes. This incompatibility further exacerbates the light scattering (fig. S2), restricting VAM to

highly transparent materials and low-resolution structures(*13*). Concurrently, severe optical crosstalk typically confines array fabrication to a single Z-axis, restricting its potential for scalable production(*14*).

Various approaches have been explored to improve resolution. Xolography(*15, 16*) utilizes intersecting light sheets, which often involves the use of customized material systems. Other optical field engineering strategies, such as holographic phase modulation(*17*) and digital incoherent synthesis of holographic light fields (DISH)(*18*) are well-suited for micro-scale fabrication and generally rely on high optical transparency. Furthermore, while these methods are highly effective at enhancing positive features, achieving comparable precision for complex negative features, such as internal microchannels, remains an ongoing challenge. Fundamentally, these limitations stem from the singular logic of existing light-based 3D printing methods: "exposure = curing"(*19*), which physically precludes the decoupling of target exposure from inevitable parasitic exposure.

To break this paradigm, we introduce Boolean Lithography (BL), rewriting photocuring into a Boolean operation logic: "initiation AND (NOT inhibition)=curing". This shifts polymerization from passive exposure dose accumulation to active dual regulation of energy accumulation and dissipation, enabling precise control over 3D photocuring boundaries. Specifically, the "AND" operation is realized via a custom positive-negative projection strategy using two orthogonally arranged optical engines, while the "NOT" operation is achieved through triplet photosensitizers that quench primary radicals via a newly identified electrostatic-enhanced single-electron transfer (EE-SET) pathway. This creates an *in situ* synchronous "additive-subtractive" manufacturing mode—one light drives additive shaping while another dictates subtractive correction—selectively suppressing parasitic curing without sacrificing VAM's exceptional build rates. As a result, BL-VAM broadens the printable window by 201%, achieves a printing resolution (43.6 μm) matching the optical resolution (50 μm), unlocks 3×3×3 spatial arrays, and enables stable printing in highly scattering (180 NTU) inks. Its broad applicability is also validated across both aqueous and oleaginous resin systems. These results establish a scalable paradigm for high-precision VAM and suggest a general strategy for mitigating parasitic exposure in other light-based manufacturing systems.

Principle of BL-VAM

To mitigate the inherent parasitic exposure in conventional VAM, we introduce the concept of executing Boolean operations on 3D light fields. Specifically, the initiation light field (wavelength λ_1) is spatiotemporally sculptured by an inhibition light field (wavelength λ_2). Governed by an "AND-NOT" logic, polymerization proceeds exclusively in regions where the initiation light is present AND the inhibition light is NOT (Fig. 1A). By synergistically modulating the spatial distributions of these two light fields, precise control over the solidifying voxels can be achieved.

Current photoinhibition mechanisms predominantly rely on bespoke photochromic molecules(*12*) or wavelength-specific bond cleavage(*20*), severely restricting their general applicability. To physically implement this logic framework universally, without the need for complex molecular synthesis, we uncover a novel EE-SET photochemical pathway. Upon 405-nm (λ_1) irradiation, the ionic photoinitiator lithium phenyl-2,4,6-trimethylbenzoylphosphinate (LAP) cleaves into a neutral carbon-centered radical (R_C) and a negatively charged phosphorus-centered radical (R_P)(*21*). The latter primarily drives propagating polymerization(*22, 23*), which constitutes the conventional photocuring pathway(*24*). Meanwhile, specific photosensitizers, such as methylene blue (MB)(*25*), thionine(*26*), eosin Y (EY)(*27*), can transition into a high-energy triplet state upon

excitation by a specific wavelength (λ_2), exhibiting a strong propensity to accept electrons(*28*). While triplet photosensitizers are traditionally paired with specific electron donors to generate reactive species, we reasoned that the primary radicals—bearing unpaired electrons—could serve as potent electron donors(*29-32*). Consequently, this electron transfer pathway can be inversely harnessed to inhibit polymerization. By selecting a positively charged triplet photosensitizer, we leverage its electrostatic affinity with the anionic phosphorus radical to confine them in close proximity. This spatial confinement accelerates the single-electron transfer (SET) process(*33-35*), passivating the active radicals into inert species. These inert species subsequently engage in termination reactions(*36*), depleting monomer radicals and halting the polymerization progression(*24*). Thus, the initiation and inhibition light independently dictate the onset and termination of photopolymerization (Fig. 1B). This EE-SET mechanism establishes a scalable chemical foundation for BL, relying entirely on accessible commercial reagents.

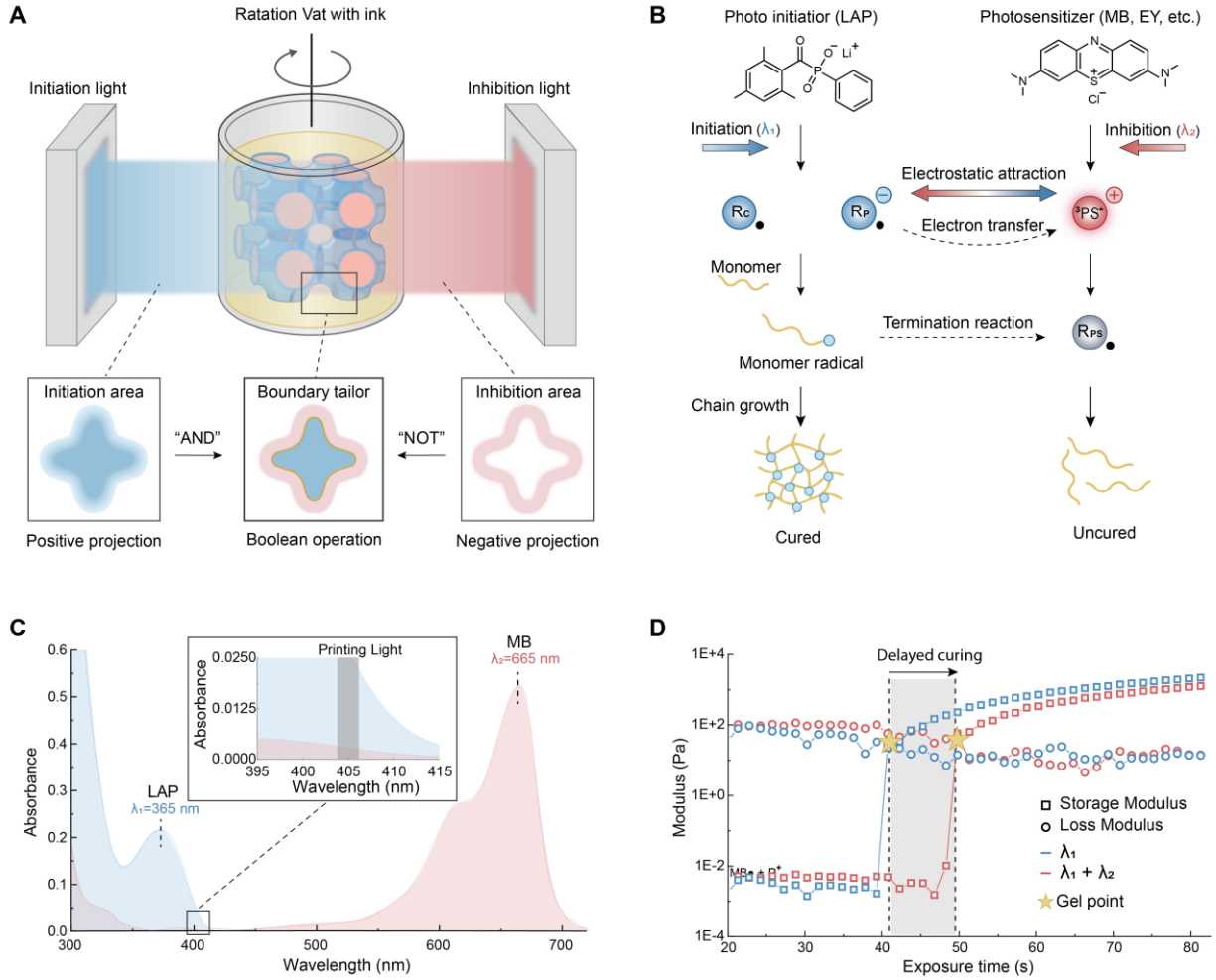

Fig.1. Framework design of BL-VAM. (**A**) Fundamental framework and optical field tailoring logic of BL-VAM. (**B**) Principles of the photoinitiation and photoinhibition pathways. (**C**) Spectral orthogonality between the photoinitiator and the photosensitizer. (**D**) Curing delay effect induced by the EE-SET pathway

Hardware implementation requires only the integration of an auxiliary inhibition module, preserving the fundamental VAM architecture without any modification. Specifically, we engineered an orthogonal "positive-negative" projection configuration, employing two

independent optical engines to deliver the initiation and inhibition light. Another fundamental prerequisite is strictly orthogonal spectral matching; the initiator and the photosensitizer must independently respond to λ_1 and λ_2 without optical crosstalk (Fig. 1C). After verifying the feasibility of multiple initiator-sensitizer combinations (fig. S4), we selected LAP (λ_1= 405 nm) and MB (λ_2 = 630 nm) for proof-of-concept demonstrations. Photorheological measurements of a poly(ethylene glycol) diacrylate (PEGDA) aqueous solution confirmed that irradiation with λ_1 + λ_2 delayed gelation time by approximately 10 seconds compared to λ_1 irradiation alone (Fig. 1D). Since typical VAM completes within tens of seconds, this 10-second delay establishes a sufficiently robust temporal window to effectively suppress parasitic exposure.

Mechanistic validation of EE-SET

To evaluate the thermodynamic basis of the SET process, the electrochemical behavior of the MB solution was analyzed via cyclic voltammetry (CV). The result revealed that under λ_2 irradiation, the redox peaks of MB shifted to more negative potentials compared with the dark state (Fig. 2A). This electrochemical shift confirms MB's transition into an excited state, providing the thermodynamic driving force to accept electrons from primary radicals. Then, to elucidate corresponding kinetic dynamics, the ultraviolet-visible (UV-Vis) absorption spectra of MB were tracked. Under standalone λ_2 irradiation, the 665 nm peak remained stable, reflecting triplet-state persistence without electron donors. Standalone λ_1 induced moderate bleaching via basal reduction. Conversely, simultaneous λ_1 + λ_2 irradiation accelerates peak decay (Fig. 2B). This spectral attenuation confirms an accelerated reaction between the λ_2-excited triplet MB and radicals, indicating its capacity to rapidly scavenge electrons from primary radicals and thereby transition into a colorless reduced state.

The role of radicals in EE-SET was analyzed via electron paramagnetic resonance (EPR) spectroscopy. Using 5,5-dimethyl-1-pyrroline N-oxide (DMPO) as a spin trap, we monitored the spin adduct signals of the LAP-MB system under specific irradiation wavelengths (Fig. 2C). In the EPR spectra, the trapped R_C yields a concentrated signal near 3500 G, whereas the R_P exhibits a broader multiplet distribution(*32, 37*). Upon normalizing the spectra to the central R_C peak, the maximum peak intensity of the peripheral RP signal decreased by 44.9% under λ_1 + λ_2 irradiation relative to λ_1 alone, confirming R_P scavenging (Fig. 2D). As a control, standalone λ_2 irradiation yielded no signals (fig. S5). Furthermore, inductively coupled plasma mass spectrometry (ICP-MS) analysis of the digested hyaluronic acid methacrylate (HAMA) hydrogels revealed a decreased phosphorus content within the dual-wavelength-polymerized networks (Fig. 2E). This elemental depletion indicates that R_P is excluded from the final crosslinked network(*24*).

Spatially controlled curing experiments using a PEGDA solution visually validated the inhibitory effect of EE-SET (fig. S6). The precursor solution, contained in a transparent quartz cuvette, was uniformly illuminated from below by a λ_1 area source, while an orthogonal λ_2 point source selectively irradiated the experimental volume. The localized region intersected by the λ_2 beam remained liquid, whereas the surrounding uninhibited area fully polymerized (Fig. 2F, movie S1). To quantify this suppression, the crosslinked and enzymatically digested HAMA hydrogels were analyzed via gel permeation chromatography (GPC). The dual-wavelength-irradiated networks exhibited a decreased average molecular weight, indicating restricted chain propagation (Fig. 2G). This restriction was substantiated by ^{1}H nuclear magnetic resonance (^{1}H NMR) (Fig. 2H) and Fourier-transform infrared (FTIR) spectroscopy (Fig. 2I) (*38*), which confirmed a higher retention of unreacted carbon-carbon double bonds in the dual-wavelength group at equivalent exposure doses.

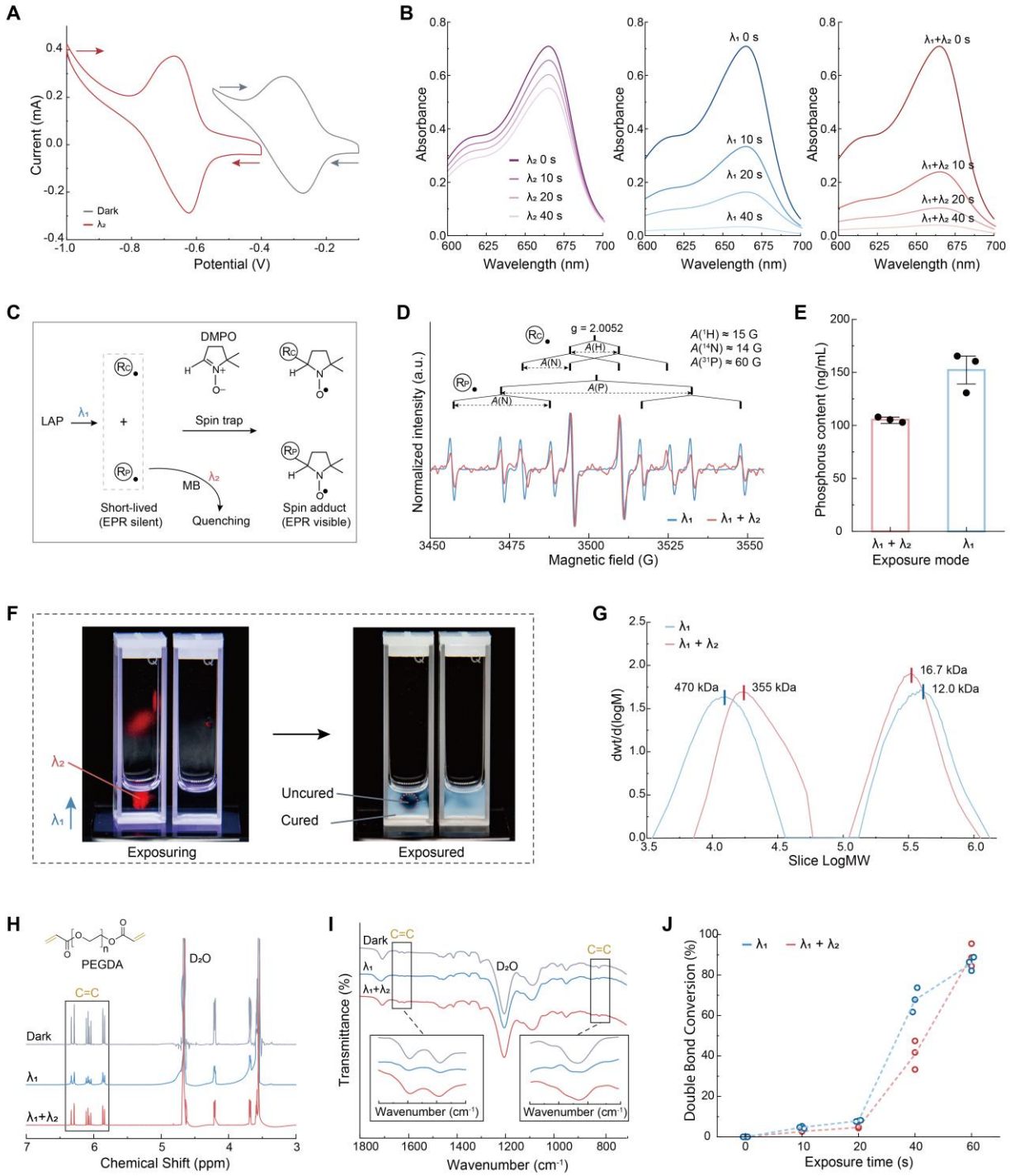

Fig.2. Mechanistic validation of EE-SET. (**A**) Shifts in the redox curves of MB under λ2 irradiation. (**B**) Evolution of the UV-Vis absorption spectra of MB-LAP under various illumination conditions. (**C**) Radical trapping utilizing DMPO. (**D**) EPR spectra of the LAP-MB system under different illumination conditions. (**E**) Elemental content of the crosslinked hydrogel quantified via ICP-MS. (**F**) Visual demonstration of the curing inhibition effect. (**G**) Molecular weight of the crosslinked hydrogel networks measured via GPC. Double-bond conversion of the hydrogels under different illumination conditions characterized by ^{1}H NMR (**H**) and FTIR (**I**). (**J**) Dynamic analysis of double-bond conversion during curing.

As controls, standalone λ_2 irradiation induced no detectable changes in ^{1}H NMR (fig. S7A) or photorheological profiles (fig. S8A). Furthermore, sequential exposure (λ_2 followed by λ_1) yielded results identical to standalone λ_1 irradiation (fig. S7B, S8B). This confirms that effective photoinhibition strictly requires the simultaneous spatiotemporal overlap of both light fields, precluding any interference from persistent photosensitizer byproducts. Finally, dynamic crosslink degree analysis revealed that dual-wavelength irradiation significantly suppresses double-bond conversion near the gelation point, although both groups ultimately converge to comparable final conversion levels upon complete curing (Fig. 2J). Mechanical tests indicated a slightly reduced Young's modulus in the dual-wavelength group (fig. S9A-B).

To validate the electrostatic enhancement of the SET process, alternative photoactive species were evaluated. Utilizing positively charged triplet photosensitizers—Rhodamine B (fig. S10A), new methylene blue (fig. S10B), thionine (fig. S10C), and water-soluble EY (fig. S10D)—polymerization inhibition was consistently observed under their respective λ_2 excitations. Conversely, the application of uncharged, alcohol-soluble EY yielded no detectable inhibition (fig. S11). Similarly, replacing the anionic LAP with neutral photoinitiators, such as VA-086 (fig. S12A) and I-2959 (fig. S12B), yielded no significant polymerization inhibition under corresponding λ_1 irradiation. Furthermore, introducing NaCl into the LAP-MB system to induce electrostatic screening partially attenuated the curing inhibition (fig. S13).

Characterization of the parameter space

In VAM, the standard concentration of LAP is typically set to 0.05% (w/v) to ensure the penetration of the initiating λ_1 light throughout the entire print volume. Upon the introduction of MB, to guarantee effective penetration of λ_2 across the same volume, the maximum MB concentration was established at 0.005% (w/v) via optical penetration assays (fig. S14). Photorheological testing was employed to precisely track the viscoelastic transition of the precursor, where the gelation point (storage modulus G' equals loss modulus G") serves as the hallmark of the transition from a liquid state to a solid crosslinked network(*39, 40*) (fig. S15). Based on this criterion, the core process parameters of BL-VAM were systematically characterized. The results indicate that a substantial curing inhibition effect (a delay of approximately 10 s) is observed when the MB concentration exceeds 0.001% (w/v), with the delay time exhibiting a positive correlation with MB concentration (Fig. 3A). Under a constant λ_1 intensity of 10 mW/cm², the threshold for λ_2 intensity was determined to be greater than 5 mW/cm² (i.e., an intensity ratio exceeding 0.5:1) to trigger effective inhibition (Fig. 3B). Ambient temperature screening revealed that the system maintains effective curing inhibition across a range of 15 to 60 °C (Fig. 3C); however, this inhibitory effect attenuates at elevated temperatures, which can be attributed to the thermal instability of MB at high temperatures.

To validate the material universality of BL, various photocurable hydrogels, including HAMA, polyether F127 diacrylate (F127DA), and dextran methacryloyl (DexMA), were tested, confirming the broad applicability in aqueous systems (Fig. 3D). Additionally, the introduction of rheological thickeners, such as hyaluronic acid and hydroxyethyl cellulose (fig. S16), yielded no significant interference with the EE-SET pathway. Furthermore, for lipid-soluble resin materials, PEGDA was employed as an amphiphilic intermediate to incorporate LAP and trace amounts of water (1% w/v) into a commercial amine-modified epoxy acrylate resin (at a mass ratio of 33%PEGDA: 66%resin: 1%water), successfully formulating a mixed-phase photocurable resin system (fig. S17). Subsequent photorheological testing confirmed that EE-SET remains effective within the lipid-soluble system.

In free-radical polymerization, oxygen competitively forms inert peroxyl radicals at a rate vastly exceeding monomer conversion(*41*). This rapid radical scavenging during initial exposure delays gelation, effectively attenuating the initiation pathway (Fig. 3E). Notably, oxygen also functions as a triplet quencher in the EE-SET system(*42*), simultaneously attenuating the photoinhibition pathway by forcing high-energy MB back to its ground state via singlet oxygen generation. Although oxygen can also slowly reoxidize the reduced leuco-MB(*43*), this hours-long process is negligible during the rapid printing window. Taken together, oxygen plays a dual-antagonistic role in the BL system—simultaneously attenuating both the photoinitiation and photoinhibition pathways. Photorheological evaluations under various gaseous atmospheres verified this dynamic characteristic: as the oxygen concentration decreases, the λ_1-driven crosslinking rate accelerates, while the λ_2-driven curing delay time extends accordingly (Fig. 3F-G). Given the enclosed nature of the printing vessel in VAM(*44*), a standard ambient atmosphere is sufficient to maintain the stable operation of the BL-VAM system.

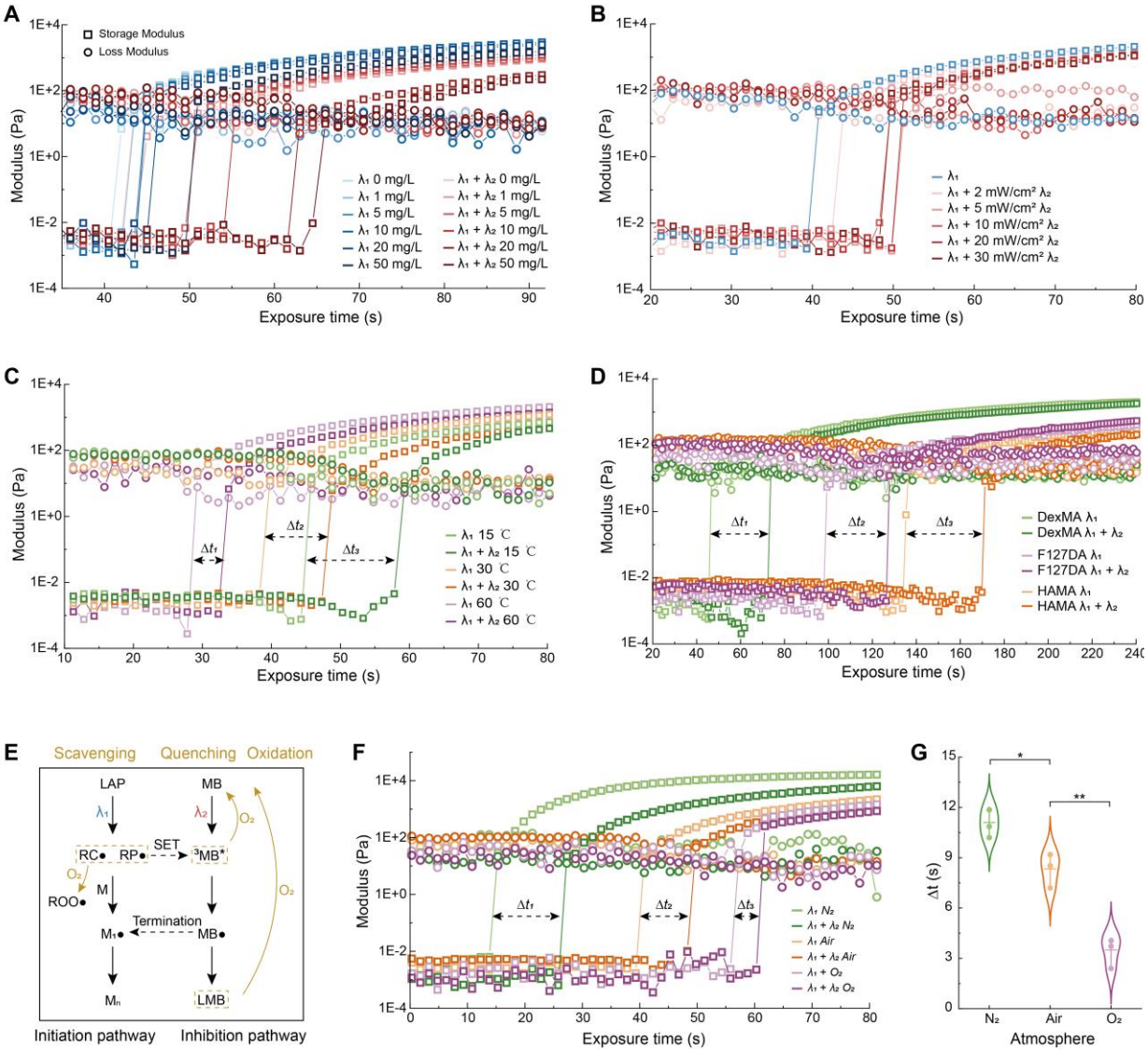

Fig.3. Characterization of the parameter space. Photorheological profiles measured at varying MB concentrations (**A**), λ_2 intensities (**B**), ambient temperatures (**C**), and across different hydrogel monomers

(**D**). (**E**) The dual role of oxygen in both the photoinitiation and photoinhibition pathways. Comparison of photorheological profiles (**F**) and gelation times (**G**) evaluated under different gaseous atmospheres.

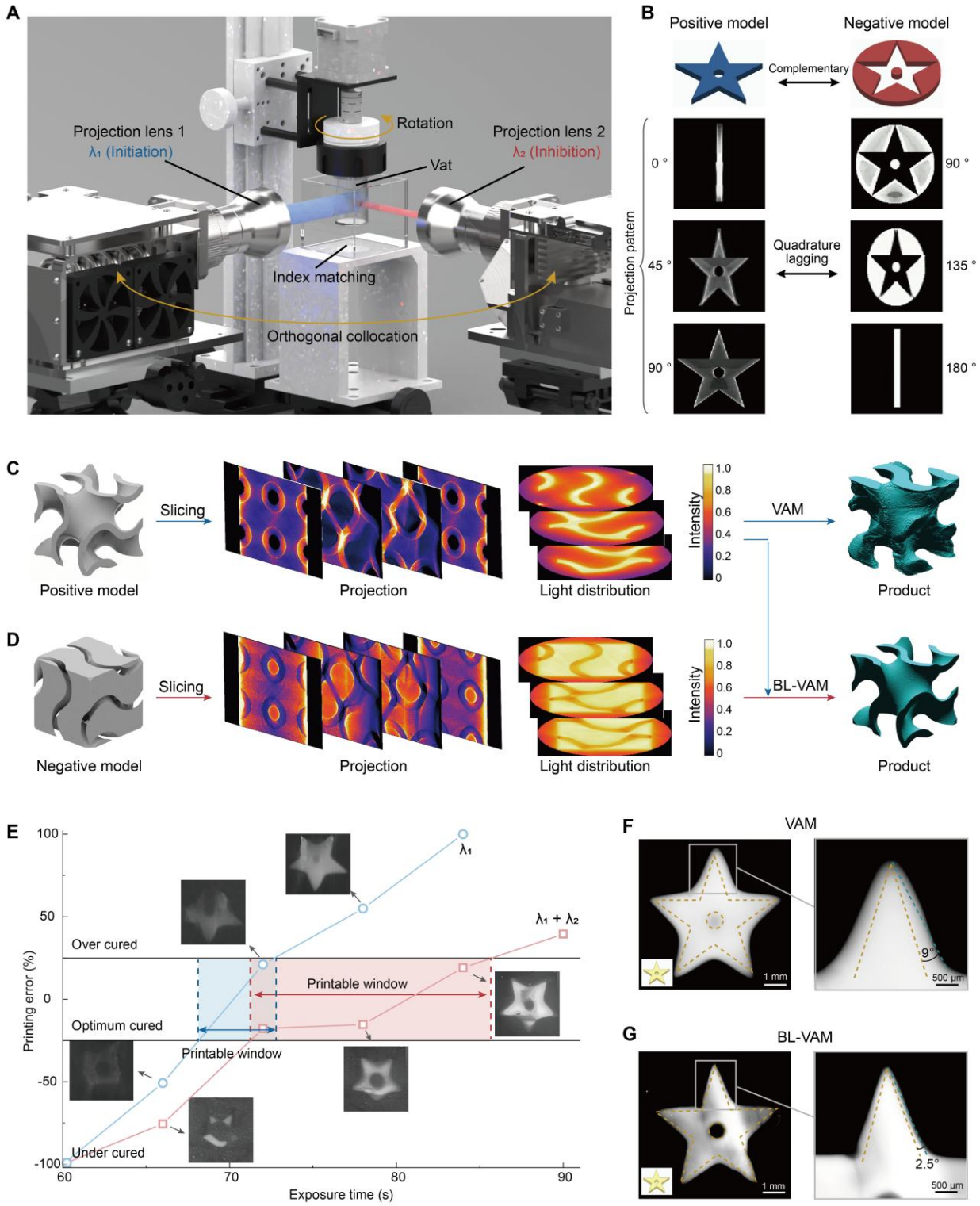

Fig.4. System architecture for enhancing printing fidelity. (**A**) Hardware architecture of the orthogonal "positive-negative" projection system. (**B**) Spatiotemporal synchronization of the positive and negative projection optical fields. Slicing and tomographic light field reconstruction for the positive

model (**C**) and the negative model (**D**). (**E**) Comparison of the printable windows between conventional VAM and BL-VAM. Structural fidelity analysis of parts fabricated by VAM (**F**) and BL-VAM (**G**).

System architecture

The BL-VAM system employs an orthogonal "positive-negative" dual-projection architecture (Fig. 4A). Two light engines, emitting at wavelengths of $\lambda_1 = 405$ nm and $\lambda_2 = 630$ nm, respectively, are arranged at a 90° angle and strictly aligned spatially via high-precision translation stages. The system is equipped with a refractive-index-matching vat to minimize interfacial optical distortion.

Meanwhile, a 90° digital rotation of the projection patterns compensates for the orthogonal projector layout, enabling strict spatiotemporal synchronization of the intersecting optical fields (Fig. 4B). Regarding model processing, the "positive model" corresponds to the target three-dimensional entity to be printed, whereas the "negative model" is generated via either a "bounding box" or "expanded body" strategy (Fig. 4C-D, fig S19). Fundamentally, serving as the spatial complement to the positive model, the negative model is designed to specifically neutralize parasitic exposure outside the target regions. Subsequently, utilizing existing open-source CAL algorithms(*8*), the positive and negative models undergo slicing and tomographic image optimization, respectively, generating the initiating and inhibiting optical field sequences for synchronized projection.

To validate the fabrication efficacy of BL-VAM, a hollow pentagram was employed as a proof-of-concept model, and the dynamic polymerization process of the PEGDA solution was recorded *in situ* via a camera. Modulation via the inhibition light field broadens the printable time window (defined by a ±25% dimensional error) by 201%, extending it from 4.6 to 13.9 s (Fig. 4E, fig S20, movie S2). Further optical microscopy characterization confirms that structures fabricated via BL-VAM exhibit significantly enhanced shape fidelity in both their positive features (solid contours) and negative features (internal voids) (Fig. 4F-G).

Experimental validation of BL-VAM

In VAM, the spatial pose of models profoundly impacts the quality of tomographic reconstruction and the ultimate fabrication precision. Typically, the primary axis of the model must be aligned parallel to the rotation axis (Z-axis). Conversely, BL-VAM exhibits better orientation flexibility, enabling high-fidelity manufacturing at arbitrary angles (Fig. 5A). For batch production, traditional VAM is limited to 1D stacking along the Z-axis to avoid optical occlusion. In-plane (X-Y) arrays often fail due to parasitic curing within inter-model gaps. By specifically suppressing parasitic exposure, BL-VAM enables 3×3×3 spatial arrays (Fig. 5B, movie S3-S4), effectively increasing fabrication throughput. Additionally, conventional VAM requires highly transparent precursors to mitigate scattering. As a demonstration, we incorporated 0.05% (w/v) fluorescent polystyrene microspheres into the PEGDA precursor—elevating turbidity to 9.78. Subsequent fabrication assays demonstrate that BL-VAM maintains robust printing performance, extending the material compatibility to scattering-intensive heterogeneous systems (fig. S21-S22).

Aqueous hydrogel and oil-soluble resin precursors were utilized to validate the capability of BL-VAM in fabricating complex 3D architectures. In hydrogels, complex geometries—including bionic sea urchins (Fig. 5C), complex lattice models (Fig. 5D), triply periodic minimal surfaces (Fig. 5E), and hollow eggshells (Fig. 5F)—were successfully fabricated, accurately replicating both sharp solid contours and minute internal voids. In resins, "The Thinker" statue (Fig. 5G), biomimetic vascular models (Fig. 5H), and structures featuring embedded complex internal channels were fabricated (Fig. 5I). Red dye perfusion and micro-computed tomography (micro-

CT) reconstruction verified the high interconnectivity and patency of the internal network. To investigate the resolution limit for negative features, we fabricated a fine microchannel in 12% (w/v) PEGDA. *In situ* monitoring revealed that while traditional VAM fails to resolve fine pores—which are typically engulfed by surrounding parasitic exposure—BL-VAM clearly resolves structural boundaries with a stable 3-s printing window (Fig. 5J, movie S5). Microscopic imaging and quantitative measurements confirmed a minimum channel size of 43.6 μm (Fig. 5K).

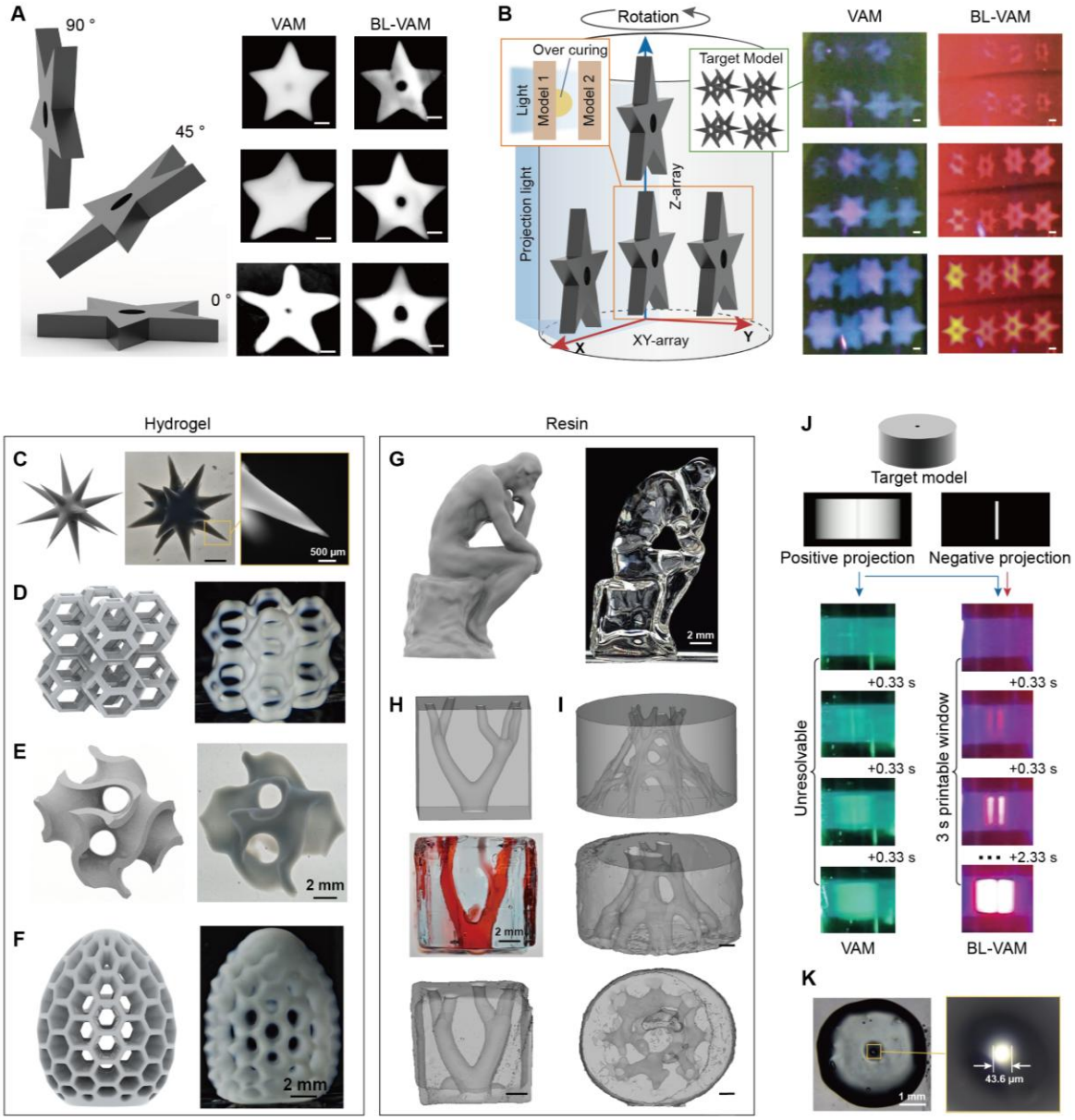

Fig.5. Experimental validation of BL-VAM. (**A**) Impact of model spatial pose on printing fidelity. (**B**) Comparison of arrayed printing capabilities. Printed results versus design models for hydrogel-based bionic sea urchins (**C**), complex lattice structures (**D**), triply periodic minimal surfaces (**E**), and hollow eggshells (**F**). Printed results versus design models for resin-based "The Thinker" statue (**G**), biomimetic vascular models (**H**), and structures embedded complex internal channels (**I**). (**J**) *In situ* optical recording of the fine pore fabrication process. (**K**) Optical micrograph revealing the minimum negative feature size achieved by BL-VAM.

Discussion

In summary, we propose an optical fabrication method, BL-VAM, which introduces the concept of Boolean operations into light field modulation. This method achieves a printing resolution (43.6 μm) commensurate with the optical resolution (50 μm) without compromising inherent volumetric build rates. Architecturally, BL-VAM requires merely the addition of a secondary projection engine, without necessitating any fundamental modifications to existing hardware architectures or the open-source CAL algorithms. Furthermore, the system is highly versatile across various hydrogel and resin formulations without demanding complex, customized chemical syntheses. By mitigating parasitic exposure, BL-VAM improves scattering tolerance (fig. S23) and orientation freedom, while simultaneously boosting production throughput.

In fact, the fundamental principles of Boolean operations are already implicitly manifested in several existing photopolymerization technologies. For instance, the dual-color intersecting initiation in Xolography(*15*), as well as super-resolution methods(*45*) relying on double exposure, essentially operate on an "AND" logic. Fundamentally, this "AND" logic relies on energy superposition, making it difficult to eliminate redundant energy accumulation in off-target regions. In contrast, the "AND-NOT"S spatial logic proposed herein functions as an energy dissipation mechanism. By actively neutralizing excess exposure doses, it provides a deterministic route to eliminate parasitic exposure. Grounded in this thermodynamic distinction, this work formally establishes the conceptual framework of BL.

The current implementation of BL via the EE-SET pathway operates within specific boundary conditions. The photochemistry relies on triplet-state photosensitizers, which, upon quenching by dissolved oxygen, generate cytotoxic reactive oxygen species(*46*). Consequently, the current system is more suited for manufacturing acellular biomimetic scaffolds rather than direct cell-laden bioprinting. Additionally, the presence of strongly charged species or complex macromolecular proteins within the precursor inks may interfere with the single electron transfer pathway, thereby potentially attenuating the photoinhibition efficacy.

Crucially, beyond VAM, BL offers a generalizable strategy to address the pervasive precision-efficiency trade-off in light-based 3D printing. Typically, voxel resolution and fabrication throughput exhibit an inversely proportional relationship—halving the minimum feature size often drastically penalizes the fabrication efficiency. BL could eradicate scattering-induced parasitic curing without extending physical exposure times, effectively shifting the entire Pareto front of the precision-efficiency curve upward. This paradigm can be translated to other light-based 3D printing methods. In SLA, beam-shaping techniques can be applied to overlap a doughnut-shaped inhibition beam around the initiation beam (akin to zero-intensity node modulation) to neutralize in situ scattering. Similarly, in DLP, the synchronized projection of complementary 2D mask patterns can effectively suppress intra-layer overcuring (fig. S24). By eradicating parasitic exposure at the fundamental mechanistic level, we believe that the BL paradigm will be broadly integrated into all scattering-limited optical manufacturing technologies, opening a promising frontier for the high-throughput, high-precision fabrication of complex 3D architectures.

References and Notes

1. F. P. W. Melchels, J. Feijen, D. W. Grijpma, A review on stereolithography and its applications in biomedical engineering. *Biomaterials* **31**, 6121–6130 (2010).
2. C.-f. He *et al.*, Printability in Multi-material Projection-Based 3-Dimensional Bioprinting. *Research* **8**, 0613 (2025).

3. S. Kawata, H. Sun, T. Tanaka, K. Takada, Finer features for functional microdevices - Micromachines can be created with higher resolution using two-photon absorption. *Nature* **412**, 697–698 (2001).
4. T. Qiao *et al.*, Bioink design for organ-scale projection-based 3D bioprinting. *Nature Protocols*, (2025).
5. S. Gu *et al.*, 3D nanolithography with metalens arrays and spatially adaptive illumination. *Nature* **648**, 591–599 (2025).
6. M. Shusteff *et al.*, One-step volumetric additive manufacturing of complex polymer structures. *Science Advances* **3**, (2017).
7. X. Zhang *et al.*, Technological progress and challenges of volumetric additive manufacturing technology. *Virtual and Physical Prototyping*, (2026).
8. B. Kelly *et al.*, Volumetric additive manufacturing via tomographic reconstruction. *Science* **363**, 1075–+ (2019).
9. C. M. Rackson *et al.*, Object-Space Optimization of Tomographic Reconstructions for Additive Manufacturing. *Additive Manufacturing* **48**, (2021).
10. C. F. He, T. H. Qiao, G. H. Wang, Y. Sun, Y. He, High-resolution projection-based 3D bioprinting. *Nature Reviews Bioengineering* **3**, 143–158 (2025).
11. J. Huh *et al.*, Combinations of photoinitiator and UV absorber for cell-based digital light processing (DLP) bioprinting. *Biofabrication* **13**, (2021).
12. N. D. Dolinski *et al.*, Solution Mask Liquid Lithography (SMaLL) for One-Step, Multimaterial 3D Printing. *Advanced Materials* **30**, e1800364 (2018).
13. D. Loterie, P. Delrot, C. Moser, High-resolution tomographic volumetric additive manufacturing. *Nat Commun* **11**, 852 (2020).
14. Y. Zhu, S. M. A. Nipu, S. Chen, X. Li, Linear volumetric additive manufacturing of polymer structures via light initiated direct growth. *Light: Advanced Manufacturing* **6**, (2025).
15. M. Regehly *et al.*, Xolography for linear volumetric 3D printing. *Nature* **588**, 620–624 (2020).
16. V. Hahn *et al.*, Light-sheet 3D microprinting via two-colour two-step absorption. *Nature Photonics* **16**, 784–791 (2022).
17. M. I. Alvarez-Castano *et al.*, Holographic tomographic volumetric additive manufacturing. *Nat Commun* **16**, 1551 (2025).
18. X. Wang *et al.*, Sub-second volumetric 3D printing by synthesis of holographic light fields. *Nature* **650**, 882–890 (2026).
19. E. Andrzejewska, Photopolymerization kinetics of multifunctional monomers. *Progress in Polymer Science* **26**, 605–665 (2001).
20. J. Foster *et al.*, Continuous Additive Manufacturing using Olefin Metathesis. *Advanced Science* **9**, (2022).
21. T. Majima, W. Schnabel, W. Weber, Phenyl‐2,4,6‐trimethylbenzoylphosphinates as water‐soluble photoinitiators. Generation and reactivity of O Ṗ(C6H5)(O−) radical anions. *Die Makromolekulare Chemie* **192**, 2307–2315 (2003).
22. M. Yang, J. Olah, Z. Benko, Addition Reactions of Phosphorus-Centered Radicals onto Olefins: Interplay Between Stability and Reactivity. *Chemistry*, e70726 (2026).
23. C. S. Colley *et al.*, Probing the Reactivity of Photoinitiators for Free Radical Polymerization: Time-Resolved Infrared Spectroscopic Study of Benzoyl Radicals. *Journal of the American Chemical Society* **124**, 14952–14958 (2002).

24. C. F. He *et al.*, Formation Theory and Printability of Photocurable Hydrogel for 3D Bioprinting. *Advanced Functional Materials* **33**, 2301209 (2023).
25. B. Thompson, A. Kumar, V. Huxter, Concentration-dependent aggregation of methylene blue acting as a photoredox catalyst. *Physical Chemistry Chemical Physics* **26**, 19900–19907 (2024).
26. G. Porcal, E. Arbeloa, S. Bertolotti, C. Previtali, Photophysics of thionine in AOT and BHDC reverse micelles. Quenching of the triplet state by aliphatic amines studied by transient absorption spectroscopy. *Journal of Photochemistry and Photobiology a-Chemistry* **346**, 187–193 (2017).
27. M. Hayakawa, T. Aoyama, A. Ouchi, Rate constant for the generation of 1O2 from commonly used triplet sensitizers: a systematic study of the wavelength effect using the ene reaction of 2,3-dimethyl-2-butene. *Arkivoc*, 81–93 (2020).
28. A. Meyer, T. Slanina, C. Yao, B. König, Metal-Free Perfluoroarylation by Visible Light Photoredox Catalysis. *Acs Catalysis* **6**, 369–375 (2016).
29. C. Dursun, M. Degirmenci, Y. Yagci, S. Jockusch, N. Turro, Free radical promoted cationic polymerization by using bisacylphosphine oxide photoinitiators: substituent effect on the reactivity of phosphinoyl radicals. *Polymer* **44**, 7389–7396 (2003).
30. C. Dursun, M. Degirmenci, Y. Yagci, S. Jockusch, N. J. Turro, Free radical promoted cationic polymerization by using bisacylphosphine oxide photoinitiators: substituent effect on the reactivity of phosphinoyl radicals. *Polymer* **44**, 7389–7396 (2003).
31. Y. Chen, W. Duan, Silver-Mediated Oxidative C-H/P-H Functionalization: An Efficient Route for the Synthesis of Benzo b phosphole Oxides. *Journal of the American Chemical Society* **135**, 16754–16757 (2013).
32. J. Lalevée, F. Morlet-Savary, M. A. Tehfe, B. Graff, J. P. Fouassier, Photosensitized Formation of Phosphorus-Centered Radicals: Application to the Design of Photoinitiating Systems. *Macromolecules* **45**, 5032–5039 (2012).
33. M. Schmitz, M. Bertrams, A. Sell, F. Glaser, C. Kerzig, Efficient Energy and Electron Transfer Photocatalysis with a Coulombic Dyad. *Journal of the American Chemical Society* **146**, 25799–25812 (2024).
34. Y. Katayama, H. Mitsunuma, M. Kanai, Lewis Acid-Conjugated Pyrene Photoredox Catalyst Promoting the Addition Reaction of α- Silyl Amines with Benzalmalononitriles. *Chemical & Pharmaceutical Bulletin* **70**, 765–768 (2022).
35. C. Cariño *et al.*, Unveiling photoinduced electron transfers in photosensitized polyoxometalates for solar energy conversion. *Chemical Science* **16**, 19493–19518 (2025).
36. N. K. Das, B. M. Mandal, Methylene blue as a retarder of free radical polymerization: 1. Polymerization of acrylonitrile, methyl methacrylate and styrene. *Polymer* **23**, 1653–1658 (1982).
37. F. Peyrot, S. Lajnef, D.-L. Versace, Electron Paramagnetic Resonance Spin Trapping (EPR–ST) Technique in Photopolymerization Processes. *Catalysts* **12**, (2022).
38. Y. Li *et al.*, Theoretical prediction and experimental validation of the digital light processing (DLP) working curve for photocurable materials. *Additive Manufacturing* **37**, (2021).
39. Y. Sun *et al.*, Modeling the printability of photocuring and strength adjustable hydrogel bioink during projection based 3D bioprinting. *Biofabrication*, (2020).
40. K. Yu *et al.*, Printability during projection-based 3D bioprinting. *Bioactive Materials* **11**, 254–267 (2022).

41. S. C. Ligon, B. Husar, H. Wutzel, R. Holman, R. Liska, Strategies to reduce oxygen inhibition in photoinduced polymerization. *Chemical Reviews* **114**, 557–589 (2014).
42. K. Sirovatka Padon, A. B. Scranton, The effect of oxygen on the three-component radical photoinitiator system: Methylene blue,N-methyldiethanolamine, and diphenyliodonium chloride. *Journal of Polymer Science Part A: Polymer Chemistry* **38**, 3336–3346 (2000).
43. Y. Galagan, W.-F. Su, Reversible photoreduction of methylene blue in acrylate media containing benzyl dimethyl ketal. *Journal of Photochemistry and Photobiology A: Chemistry* **195**, 378–383 (2008).
44. Q. Wu *et al.*, Tomographic Volumetric Bioprinting: From Bioinks Design to Resolution Enhancement. *Bio-Design and Manufacturing*, (2025).
45. Y. Bauckhage, A. Heinrich, B. L. Lee, J. Ehmke, Curing subpixel structures for high-resolution printing of translucent materials using standard DLP-projectors. *Emerging Digital Micromirror Device Based Systems and Applications XII*, (2020).
46. K. R. Weishaupt, C. J. Gomer, T. J. Dougherty, Identification of singlet oxygen as the cytotoxic agent in photoinactivation of a murine tumor. *Cancer Research* **36**, 2326–2329 (1976).

Acknowledgments: We thank the Analysis and Testing Center of Zhejiang University for their assistance with EPR, GPC, NMR, and other measurements.

Funding:
National Natural Science Foundation of China 52325504 (Y.H.)
National Natural Science Foundation of China 52235007 (Y.H.)
National Natural Science Foundation of China U25D9019 (Y.H.)
National Natural Science Foundation of China T2121004 (Y.H.)
National Key Research and Development Program of China 2024YFB4607700 (Y.H.)
National Key Research and Development Program of China 2025YFF0521600 (Y.H.)
Key R&D Program of Zhejiang 2024SSYS0027 (Y.H.)
Fundamental and Interdisciplinary Disciplines Breakthrough Plan of the Ministry of Education of China JYB2025XDXM210 (Y.H.)

Author contributions:
Conceptualization: C.H. Q.W. Q.Y.
Methodology: Q.Y., B.Y., T.Q., Y. G.
Investigation: X.Z. Y.S., G.L.
Visualization: C.H., T.Q.
Funding acquisition: Y.H.
Project administration: Y.H., H. Y.
Supervision: Y.H., H. Y.
Writing – original draft: C.H.
Writing – review & editing: C.H., Q.W. Y.H.

Competing interests: Authors declare that they have no competing interests.

Data, code, and materials availability: All data are available in the main text or the supplementary materials.

Supplementary Materials
Materials and Methods
Figs. S1 to S24

Tables S1 to S2
Movies S1 to S5